First Observation of Chromospheric Waves in a Sunspot by DKIST/ViSP: The Anatomy of an Umbral Flash

Ryan J. French[1,2] , Thomas J. Bogdan[1], Roberto Casini[3] , Alfred G. de Wijn[3] , and Philip G. Judge[3]
[1] National Solar Observatory, 3665 Innovation Drive, Boulder, CO 80303, USA
[2] Mullard Space Science Laboratory, University College London, Dorking, RH5 6NT, UK
[3] HAO, National Center for Atmospheric Research, P.O. Box 3000, Boulder, CO 80307-3000, USA

Abstract

The Visible Spectro-Polarimeter of the NSF Daniel K. Inouye Solar Telescope collected its Science Verification data on 2021 May 7–8. The instrument observed multiple layers of a sunspot atmosphere simultaneously, in passbands of Ca II 397 nm (H line), Fe I 630 nm, and Ca II 854 nm, scanning the region with a spatial sampling of $0{.}''041$ and an average temporal cadence of 7.76 s, for a duration of 38.8 minutes. The slit moved southward across the plane of sky at $3.83 \, \mathrm{km \, s^{-1}}$. The spectropolarimetric scans exhibit prominent oscillatory "ridge" structures that lie nearly perpendicular to the direction of slit motion (north to south). These ridges are visible in the maps of line intensity, central wavelength, line width, and both linear and circular polarization. Contemporaneous Atmospheric Imaging Assembly observations indicate that these ridges are purely temporal in character and are likely attributed to the familiar chromospheric 3 minute umbral oscillations. We observe in detail a steady umbral flash near the center of the sunspot umbra. Although bad seeing limited the spatial resolution, the unique high signal-to-noise ratio data enable us to estimate the shock Mach numbers (≈ 2), propagation speeds ($\approx 9 \, \mathrm{km \, s^{-1}}$), and their impacts on the longitudinal magnetic field ($\Delta B \approx 50$ G), gas pressure, and temperature ($\Delta T / T \approx 0.1$) of subshocks over 30 s. We also find evidence for rarefaction waves situated between neighboring wave train shocks. The Ca II 854 nm line width is fairly steady throughout the umbral flash, except for a sharp $1.5 \, \mathrm{km \, s^{-1}}$ dip immediately before, and a comparable spike immediately after, the passage of the shock front. This zigzag in line width is centered on the subshock and extends over $0{.}''4$.

Unified Astronomy Thesaurus concepts: Active solar chromosphere (1980); Solar chromosphere (1479); Shocks (2086); Solar oscillations (1515); Sunspots (1653); Solar active region magnetic fields (1975); Spectro-polarimetry (1973)

1. Introduction

Well over half a century since their discovery by Beckers & Tallant (1969) and Schultz & White (1974), our interest in umbral flashes continues unabated. They remain one of the most striking dynamical chromospheric phenomena, with roots that extend deep into the umbral photosphere, possibly as far as the subsurface magnetoconvection. They span numerous density scale heights and couple distinct atmospheric layers. They provide a means of delivering mechanical energy to the optically thin chromosphere, transition region, and lower corona. The extensive monographs and reviews by Thomas & Weiss (2012), Weiss & Proctor (2014), and Khomenko & Collados (2015) provide exhaustive summaries and analyses of the research on umbral flashes through the first decade of the 21st century. For more recent efforts, from both observational and theoretical perspectives, one should consult, e.g., Madsen et al. (2015), Löhner-Böttcher (2016), Song et al. (2017), Kuźma et al. (2017a, 2017b), Felipe et al. (2018), Houston et al. (2018), Stangalini et al. (2018), Joshi & de la Cruz Rodríguez (2018), Anan et al. (2019), Bose et al. (2019), Henriques et al. (2020), Houston et al. (2020), Yurchyshyn et al. (2020), Stangalini et al. (2021a, 2021b), Felipe et al. (2021), Sadykov et al. (2021), Snow & Hillier (2021), and

Molnar et al. (2021). The following earlier papers are also valuable and particularly germane to what follows: Lites (1992), Centeno et al. (2006), Pietarila et al. (2006, 2007), Centeno et al. (2009), Bard & Carlsson (2010), and Felipe et al. (2014).

The present contribution to the subject adds to this body of knowledge by providing a unique glimpse at high spatial, spectral, and temporal resolution of 10 minutes in the hour or two lifetime of a mature umbral flash. This is achieved by employing the inaugural Science Verification (SV) data from the Visible Spectro-Polarimeter (ViSP; De Wijn et al. 2022), attached to the NSF Daniel K. Inouye Solar Telescope (DKIST; Rimmele et al. 2020).

ViSP is one of the first-light instruments of DKIST. Here, we analyze spectropolarimetric data that were obtained by ViSP during its SV campaign on 2021 May 8. ViSP uses three spectral arms and cameras to measure the full state of polarization (Stokes I, Q, U, and V) simultaneously over three different spectral windows. For SV, the instrument was configured to observe simultaneously in the passbands of the photospheric lines of Fe I around 630 nm and of the two chromospheric resonance lines of Ca II at 397 nm (the H line) and 854 nm (the second line of the IR triplet). The telescope was pointed to the northernmost sunspot of AR 12822 (the only active region on the solar disk at the time), near the northeast limb of the Sun. The line of sight (LOS) is inclined 63° ($\mu \approx 0.45$) from the sunspot's zenith, and is tilted 23° off the east–west direction.
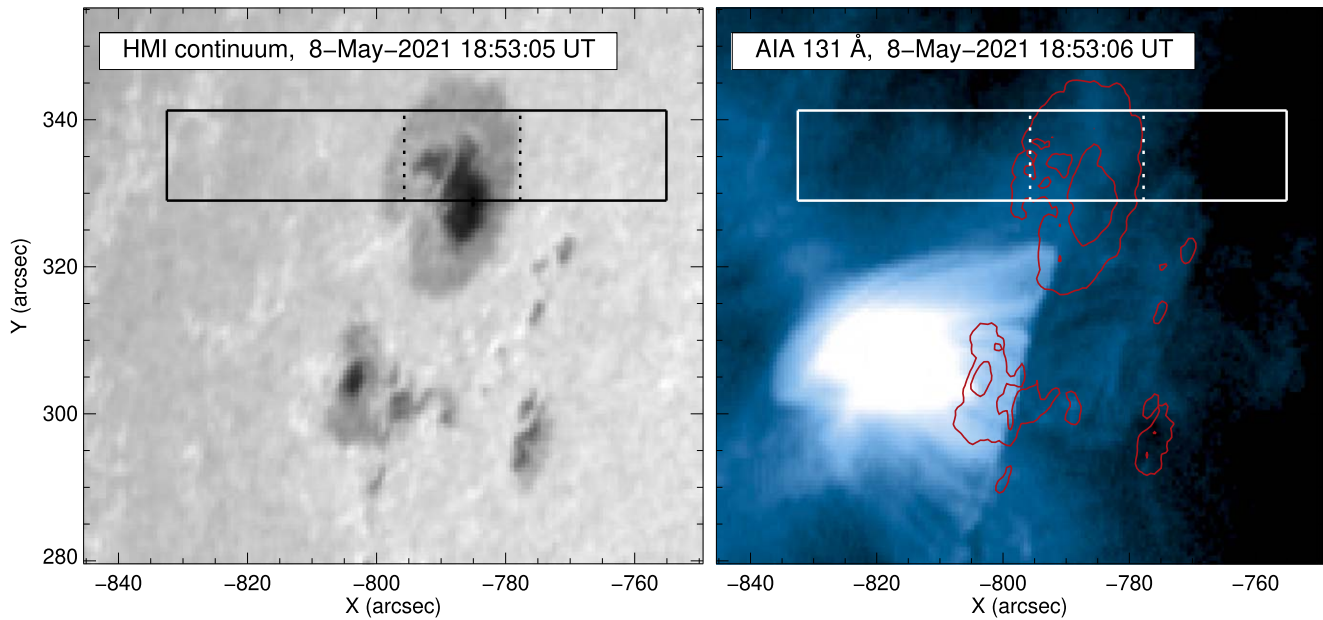
Figure 1. Left: HMI continuum showing AR 12822. The solid black rectangle marks the ViSP FOV. The dashed inset box shows the cropped FOV employed in Figure 3. Right: AIA 131 Å observations showing the solar flare in progress. As in the left panel, the solid/dashed white rectangles show the full/cropped ViSP FOVs. The red contours mark the sunspot location, as seen in the HMI continuum (left panel). The bright feature in the right panel shows the flare loops of a C-class flare peaking prior to the beginning of the ViSP observations.

2. Observations

The ViSP polarimetric scan ran from 18:52:39 to 19:31:19 UT on 8 May 2021. It consisted of 300 contiguous slit positions, separated by a slit width of $0''041$. It covered an angular extent of $12''3$ in the north–south direction. The field of view (FOV) covered by the lowest-magnification spectral arm of ViSP (vcc1) is shown in Figure 1. The extent of the FOV along the slit, and the corresponding spatial sampling by the detector, are different for the three spectral arms: $75''9$ with $0''030 \, px^{-1}$ for camera vcc1 (Fe I), $62''3$ with $0''024 \, px^{-1}$ for camera vcc2 (Ca II H line), and $49''4$ with $0''019 \, px^{-1}$ for camera vcc3 (Ca II 854 nm).

The dwell time for one slit position was 7.58 s, consisting of 25 modulation cycles of 10 states each, at a camera frame rate of 33 Hz. Because of the different intensity levels and instrument throughput values of the three spectral channels, the duty cycles of the three cameras were dramatically different, with the Fe I spectral window being integrated only 20% of the time, with 6 ms exposures. The two Ca II spectral lines were observed with a 66% duty cycle (20 ms exposures), to build a sufficient signal-to-noise ratio in the chromospheric Stokes Q, U, and V signals. After integration, the slit was advanced by one full slit width ($0''041$) for a new integration. Each of the 300 steps took 0.18 s, resulting in a time interval between slit positions of 7.76 s, for a total raster duration of 38.8 minutes. For the observations that we analyze here, the ViSP FOV was rastered over 300 steps, with a total scan time of 38.8 minutes. This corresponds to an average slit speed projected onto the plane of sky (POS) of $v_s = 3.83 \, km \, s^{-1}$.

The FOV covered by the ViSP scan is marked in Figure 1, relative to the Helioseismic and Magnetic Imager (HMI; Schou et al. 2012) white-light continuum and the Atmospheric Imaging Assembly (AIA; Lemen et al. 2012) EUV 131 Å images. Shortly before the start of the ViSP data acquisition, a C8.6-class solar flare occurred to the southeast of the active region. The bright feature in the right panel of Figure 1 marks the location of the flare loops, which peaked in emission at 18:45 UT. The northernmost footpoint of the flare loops intersects the penumbra of the larger sunspot observed by ViSP. Unfortunately, the short temporal duration and spatial coverage of the scan make it impossible to distinguish between flare-induced sunquakes and ubiquitous subphotospheric umbral wave sources in AR 12822—see, e.g., Kosovichev & Sekii (2007), Besliu-Ionescu et al. (2017), and Millar et al. (2021). A cursory examination of the contemporaneous HMI and AIA data also fails to identify any obvious oscillatory variations that can be unequivocally attributed to the flare.

For the analysis that follows, we restrict our attention to the cropped portion of the FOV that lies above the sunspot, where strong magnetic fields and sensible polarization signals should be present. The two vertical dashed lines near $X = -795$ and $X = -775$ mark the east–west boundaries of this region of interest (ROI).

2.1. Data Reduction

Figure 2 displays a typical spectropolarimetric data cross section obtained with the vcc3 camera. A robust oscillatory signal is present in all four Stokes parameters. The intensity profile consists of a narrow Gaussian core ($\Delta\lambda \approx 20 \, km \, s^{-1}$) and broad Lorentzian wings.

During the 2021 May 8 SV observations, a slight defocusing of the ViSP collimator caused the appearance of considerable astigmatism for spectral configurations that were significantly away from Littrow. While vcc1 practically did not suffer any spectral defocus, because of its proximity to the Littrow configuration ($3°31$), the spectral resolutions of cameras vcc2 and vcc3 (respectively, $7°52$ and $20°07$ from Littrow) were significantly impacted. Therefore, we did not attempt a full inversion of the Ca II 854 nm Stokes profiles. Instead, we simply applied a single Gaussian fit to the core and near wings of the intensity and $I \pm V$ profiles, to estimate the line core intensity, central wavelength, line width, and Zeeman splitting. A representative Gaussian fit is presented in Figure 2.
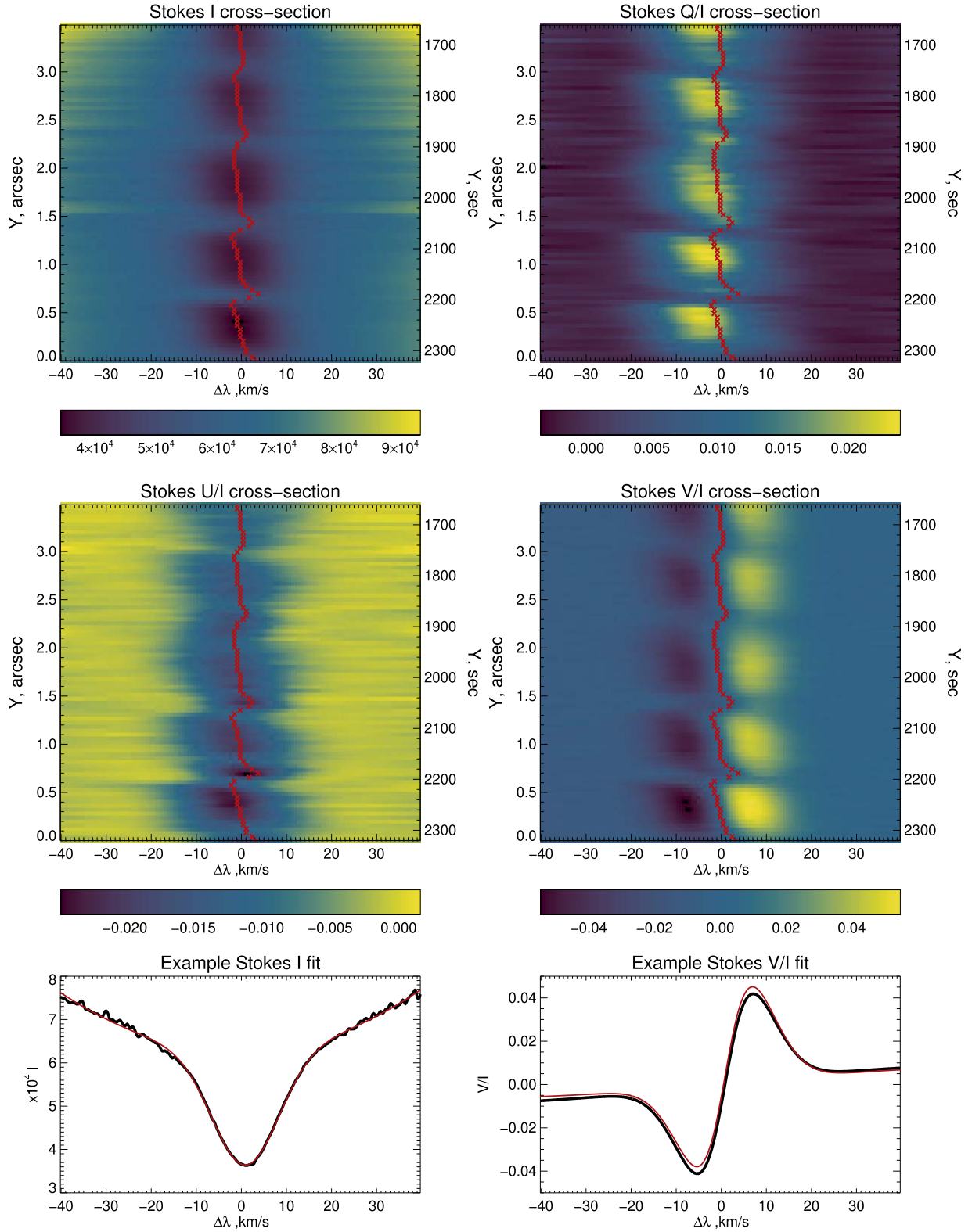
Figure 2. Full Ca II 854.2 nm spectral data of the fractional stokes parameters observed at the *X* position and along the *Y* range, corresponding to the magenta dashed line in Figure 3. The red line tracks the center of gravity of Stokes *I*. The bottom panels show an example fit (red lines) to the Stokes *I* and V/*I* data (black lines), for the spectra at *Y* = 2150 s in the top panels.

Assuming that the line centers of Stokes *I*, *Q*, and *U* occur close to the same wavelength position, the Gaussian fit also provides the positions and values of the peak Stokes *Q* and *U* emissions. This assumption holds for the majority of the FOV, but has limitations that are discussed in Section 2.2. From these linear

polarization measurements, we calculate the linear polarization degree and azimuth:

$$P = \frac{\sqrt{Q^2 + U^2}}{I},$$

(1)

$$\Phi = \frac{1}{2} \arctan \frac{U}{Q}. \qquad (2)$$

When the linear polarization is dominated by the Zeeman effect, the azimuth Φ also gives the direction of the magnetic field projected onto the POS (with a 180° ambiguity). The circularly polarized Stokes V signals yield the longitudinal magnetic field strength $B_{LOS} \equiv B \cos \Theta$, where Θ is the angle between the magnetic field vector and the LOS. A simple application of the weak-field approximation (e.g., Landi Degl'Innocenti & Landolfi 2004; Centeno 2018) appears to be adequate for providing good profile fits down to the noise level of the polarized signal (about 0.2% of Stokes I, in these observations), and was therefore used to estimate B_{LOS}.

A proper description of the atmospheric dynamics at the time of the ViSP observations requires the adequate wavelength calibration of the spectral data. Because of the visibility of many telluric (i.e., from Earth atmosphere's) molecular lines in the Fe I 630 nm spectral range, this is rather easily achieved for the vcc1 data. In contrast, the lack of strong telluric lines in the Ca II 854 nm spectrum makes a precise wavelength calibration of the vcc3 data more difficult. The significant spectral smearing of these data due to the ViSP astigmatism further complicates the matter. In order to arrive at a meaningful estimation of the chromospheric dynamics in the ViSP data, we followed the following procedure:

1. We identified a small ($\sim 3'' \times 4''$) quiet sun (QS) region to the east of the sunspot, where the photospheric dynamics are dominated by granulation, resulting in highly symmetric distributions of positive and negative Doppler shift amplitudes for the lines of Fe I at 629.8 nm and 630.1 nm, with practically zero mean LOS velocity over the region. Referencing both lines to the O2 telluric line at 629.8 nm, we estimated a photospheric blueshift of 1.65 km s^{-1}, consistent with the solar rotational velocity expected at the heliocentric coordinates of the observations.

2. We determined the center of gravity of the Fe I 853.8 nm line in the vcc3 data, and assumed it to be at rest with the photosphere probed by the Fe I lines in vcc1.

3. Finally, we referenced the center of gravity of the chromospheric Ca II 854.2 nm line to the photospheric reference of the Fe I 853.8 nm line.

The result of this wavelength calibration was that the zero-velocity reference of the Ca II 854.2 nm Doppler map in Figure 3, averaged over the entire map, was redshifted by about 1.53 km s^{-1}, with respect to the QS photosphere.

Recent work by Felipe et al. (2021) has suggested that magnetic field oscillations should not easily be detected with the Ca II 854 nm line. However, because of the sunspot's location close to the limb, the B_{LOS} measurements derived from Stokes V need not necessarily relate to changes in $|\boldsymbol{B}|$, but may well contain fluctuations in field orientation.

Figure 3 shows data from the ViSP polarization scan over the sunspot ROI indicated in Figure 1. The top row displays the intensity in the core of the photospheric Fe I 630 nm line and its LOS Doppler velocity. The second row provides the same for the chromospheric Ca II 854 nm line, while derived magnetic parameters are presented in rows two to four. Finally, the Ca II H 397 nm intensity is presented in the bottom panel.

The thin black/white contours indicate the approximate location of the umbra–penumbra boundary, determined from the Fe I 630 nm line intensity. This is the boundary between the umbra and the penumbra at the photosphere. The Ca II resonance lines are expected to form 700–1400 km above this line. Owing to the large inclination of the LOS, the projection onto the POS will shift the position of the Ca II signal directly above the Fe I signal some half to one arcsecond to the east–northeast. Wavelength-dependent atmospheric refraction will also shift the chromospheric and photospheric signals onto the POS. A light bridge separates the east satellite umbra from the larger central umbra. Present in the east (left) umbra is the vertical ViSP hairline—used for calibration between the instrument cameras.

In Figure 3, the rastered ViSP data obtained at each value of X are plotted in Y against both the slit position (left axis) and the time of the data acquisition (right axis). Convenient origins in time and the north–south slit position have been selected to facilitate the analysis and display. We use both coordinates interchangeably in what follows, to emphasize that the ViSP scan via a stepped slit necessarily mixes north–south spatial and temporal variations.

2.2. Summary of the Scans

The sunspot structure is readily apparent in the photospheric Fe I 630 nm intensity plot, showing the larger central and smaller east satellite (left) umbrae (also seen in HMI; Figure 1), separated by a thin light bridge. The surrounding penumbra is visible to the north and west (right) of these regions. There is no quiet Sun in our ROI. The Doppler velocity scans exhibit the expected Evershed flow in the photosphere and the reverse chromospheric inflow from above (e.g., Teriaca et al. 2008).

Prominent in the Ca II scans are a series of nested ridges, running almost parallel to the horizontal east–west direction across the image. These ridges are striking in the Doppler velocity and P scans. They are also present in line width, azimuth, B_{LOS}, and intensity. We see these same ridges in the H-line intensity. The average north–south separation of these ridges in Y is on the order of $0''5$. A second, more widely separated, set of horizontal ridges is also discernible in the Fe I scans. Their north–south spacing is slightly in excess of $1''$. Both sets of ridges are not strictly horizontal, but they are well resolved over 300 pixels, from north to south, and highly structured—exhibiting both curvature and variation in brightness/thickness from east to west.

Observations of similar oscillatory ridge-like structures, sometimes referred to as "herringbone" patterns, were first observed in the photosphere in works including those by Thomas et al. (1984) and Lites et al. (1998), and later in the chromosphere, with the Dunn Solar Telescope / Horizontal Grading Spectrograph, by Balasubramaniam et al. (2008).

The moving slit yields an image scan that may be neither purely temporal nor spatial, but could be a mixture of the two. It is not possible to determine from these observations alone whether the ridges originate from a large-scale coherent temporal pulsation of the entire umbra, or from the moving slit passing over a static spatial undulation, or from a sinusoidal disturbance progressing northward or southward across the sunspot. Previous observations of "herringbone" ridges have been captured by sit-and-stare measurements, which produce images of x against t. Because ViSP's moving slit creates images convolving spatial and temporal information in the
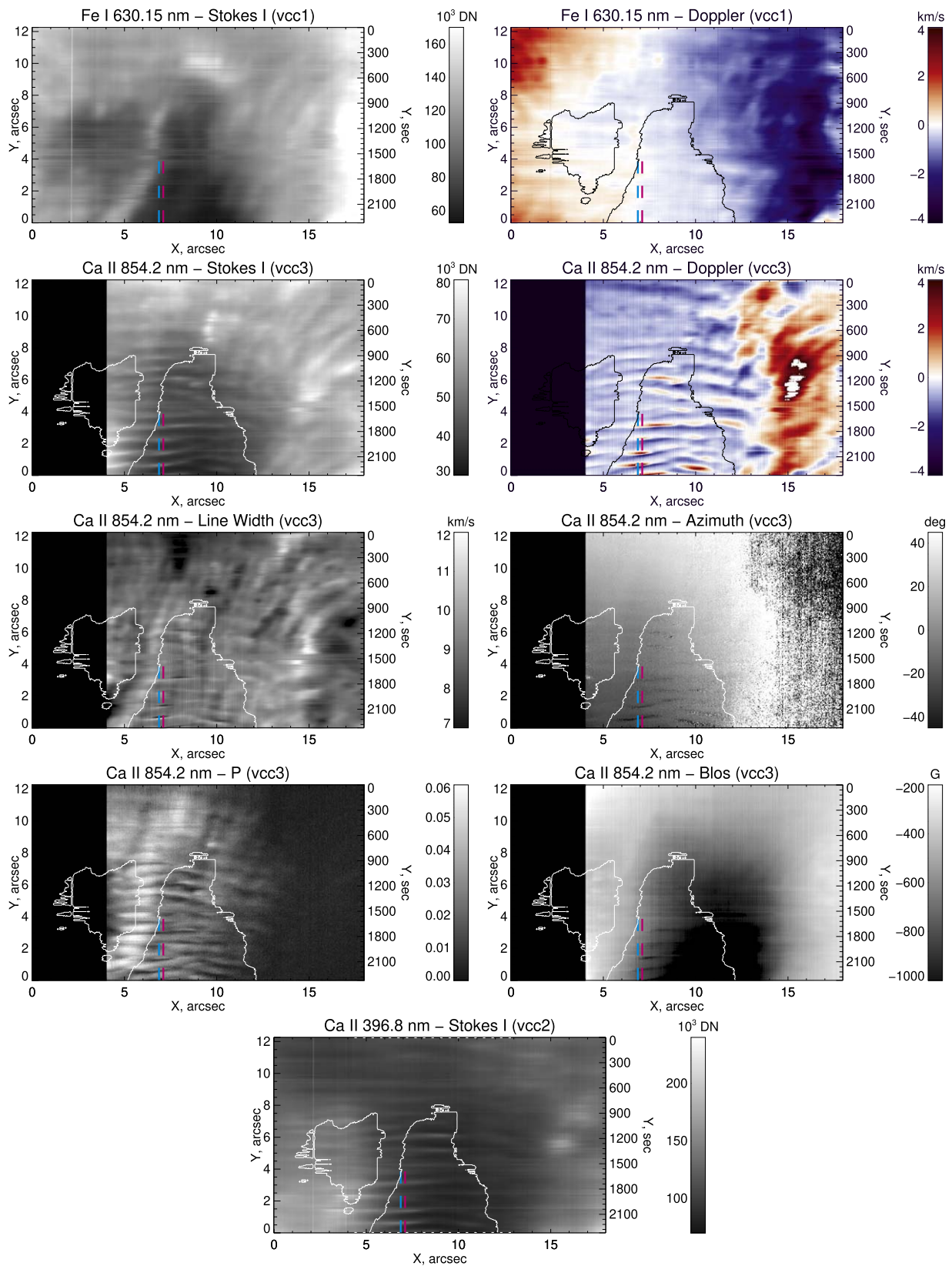
Figure 3. Active region scans from the ViSP SV campaign. The plots show cropped subsets of the full FOV, as shown in Figure 1. Each image is labeled with the spectral line and observed parameter. The dashed cyan and magenta lines show the locations of the umbral flash cross sections examined in Figure 4. The solid white/ black contours indicate the location of the sunspot umbra, as determined from the Fe I 630 nm intensity (top left panel). We omit Ca II 854.2 data below 4″, due to artifacts of poor fits in this region.

vertical axis (creating an image of x against y and t), we lay out an argument in this section that the ridges observed by ViSP are not spatially resolved structures, but are temporally resolved, similar to the previous sit-and-stare observations.

Consider a progressive oscillatory disturbance moving northward across the POS at a speed c with a spatial wavelength λ_c and a temporal period T_c. The relative velocity between the average southward speed of the stepped moving slit and the progressive disturbance determines the resulting separation of the ridges in Y. The relationships between the true (subscript "c") and observed (no subscript) wavelengths and periods (λ_c, λ and T_c, T, respectively) are

$$\frac{v_s + c}{c} = \frac{T_c}{T} = \frac{\lambda_c}{\lambda} \frac{v_s}{c}, \tag{3}$$

$$c = \frac{v_s}{T_c/T - 1} = v_s\left(\frac{\lambda_c}{\lambda} - 1\right). \tag{4}$$

The observed period T and wavelength λ are related by $\lambda = Tv_s$, where λ is the physical distance between the ridges on the ViSP scans and T is the time between the observations of the ridges. For oscillatory disturbances progressing southward, one simply replaces c with $-c$ in these expressions.

Notice that in the extreme case of a coherent spatial pulsation of the entire sunspot (λ_c, $c \to \infty$), the moving slit records the true period $T = T_c$. Likewise, for a static spatial undulation ($T_c = \infty$), the moving slit returns the true wavelength $\lambda = \lambda_c$. Between these two extremes, neither the recorded wavelength nor period will match their true POS values.

To distinguish spatial from temporal behavior, we compare the ViSP observations with contextual (contemporaneous) observations of the photosphere/chromosphere obtained by HMI (intensity and Doppler measurements) and AIA (304 Å, 1600 Å, and 1700 Å). These data have poorer spatial and temporal (per slit position) resolutions, but they have the advantages of not mixing the spatial and temporal information and extending (in both space and time) well beyond the ViSP scan. These data indicate fixed and spatially coherent patches of brightness oscillations in the sunspot umbra. This is entirely consistent with the usual behaviors of chromospheric 3 minute umbral oscillations (Khomenko & Collados 2015). Because the period of the AIA brightness oscillations matches the period of the oscillations observed by ViSP, the ViSP ridges are not Doppler shifted by the moving slit. This reveals that the ridges do not arise from spatially resolved waves traveling across the POS, but are instead purely temporal in character, as the ViSP slit moves over the pulsating region.

Because of their spatially coherent temporal and periodic nature, the ridges observed by ViSP cannot be a result of fine spatial structures within the umbra, such as intermixing hot and cool plasma elements (Socas-Navarro et al. 2000, 2009), filamentary structures (Socas-Navarro et al. 2009), two-component umbral structures (Centeno et al. 2005; de la Cruz Rodríguez et al. 2013), small-scale dynamic fibrils (Rouppe van der Voort & de la Cruz Rodríguez 2013), cool jet-like structures (Yurchyshyn et al. 2014), etc.

In the penumbra to the northwest of the umbra, the ridges are much broader and have a significant tilt relative to the X- and Y-directions. Here, our slit is probably sampling some combination of temporal and spatial variability that is appropriate to running penumbral waves.

3. The Umbral Flash

Figure 4 provides a closer look at a portion of the chromospheric ridge structure. Here, we plot a north–south cross section through the Ca II parameters along the dashed cyan and magenta line segments that are plotted in Figure 3. The spectropolarimetric cross sections for the magenta line segment appear in Figure 2. The lower axis of Figure 4 uses the temporal Y coordinate for the data acquisition and the upper axis uses the north–south spatial position of the slit at the time the data were obtained. With the exception of the Doppler velocity, the parameters have all been detrended by a polynomial fit, to suppress gradual variations across the ROI and to highlight the oscillatory signal. We also note that within this region, the line center of Stokes Q differs from Stokes I by about $3\,\mathrm{km\,s^{-1}}$, as shown in Figure 2. The line centroids of Stokes U and V still follow I.

These data show a particularly revealing example of a chromospheric umbral flash, with the wave train of shocks and rarefactions present in most of the Ca II parameters. For the chromospheric intensities, the extended shock compressions and intervening rarefaction cross sections are broad, well resolved, and symmetric about peaks and valleys. The dashed vertical lines in Figure 4 show the approximate locations of the shocks as identified by eye. The Ca II 854 nm Doppler and line width time series differ significantly from the intensity profiles. Instead of symmetric rise and fall profiles, we see a steep rise and a precipitous fall, characteristic of a thin embedded subshock. Indeed, the largest excursion near $Y = 2200$ s occurs across just 4 Y-pixels/time steps. The line width shows a somewhat broader zigzag about the subshock.

In the magenta cross section, the LOS magnetic field (i.e., Stokes V) oscillates 180° out of phase with the intensity parameters. The azimuth and linear polarization are also well correlated with the subshock, but have lower signal-to-noise ratios. There is a hint that they exhibit a negative spike at the greatest positive excursion of the Doppler width (equivalently, the negative excursion of the Doppler velocity).

A careful examination of the contemporaneous AIA and HMI data indicates that the umbral flash is confined to Y-values less than $3''$–$4''$, and that it has been oscillating there with a slowly varying temporal frequency throughout the duration of the ViSP data acquisition. The increase in the amplitude of the oscillation, from left to right in Figure 4, is consistent with the slit moving southward into the stronger core of this stationary, steady umbral flash. The temporal oscillation frequency present in Figure 4 is the same as that obtained from the AIA data during this epoch, meaning that it has not been Doppler shifted by the moving ViSP slit (Equation (4)). This is consistent with the umbral flash oscillating in place over a fixed spatial region near the center of the umbra. In other words, the motion of the slit does not shift the observed frequency from the true oscillation frequency. The spatial wavelength (bottom abscissa scale), however, is purely an artifact of the sit–stare–step method, and is given by T_c/v_s.

It is possible to estimate the parameters for these shocks. For example, let us consider the blue curve in the neighborhood of $Y = 2200$. We find the peak POS preshock downflow velocity at $Y = 2190$ to be $5.22\,\mathrm{km\,s^{-1}}$. The postshock upflow velocity is $1.70\,\mathrm{km\,s^{-1}}$. Dividing by the cosine of the inclination angle (0.443), and assuming that the motions are along a vertical magnetic flux tube near the center of the umbra, we obtain a
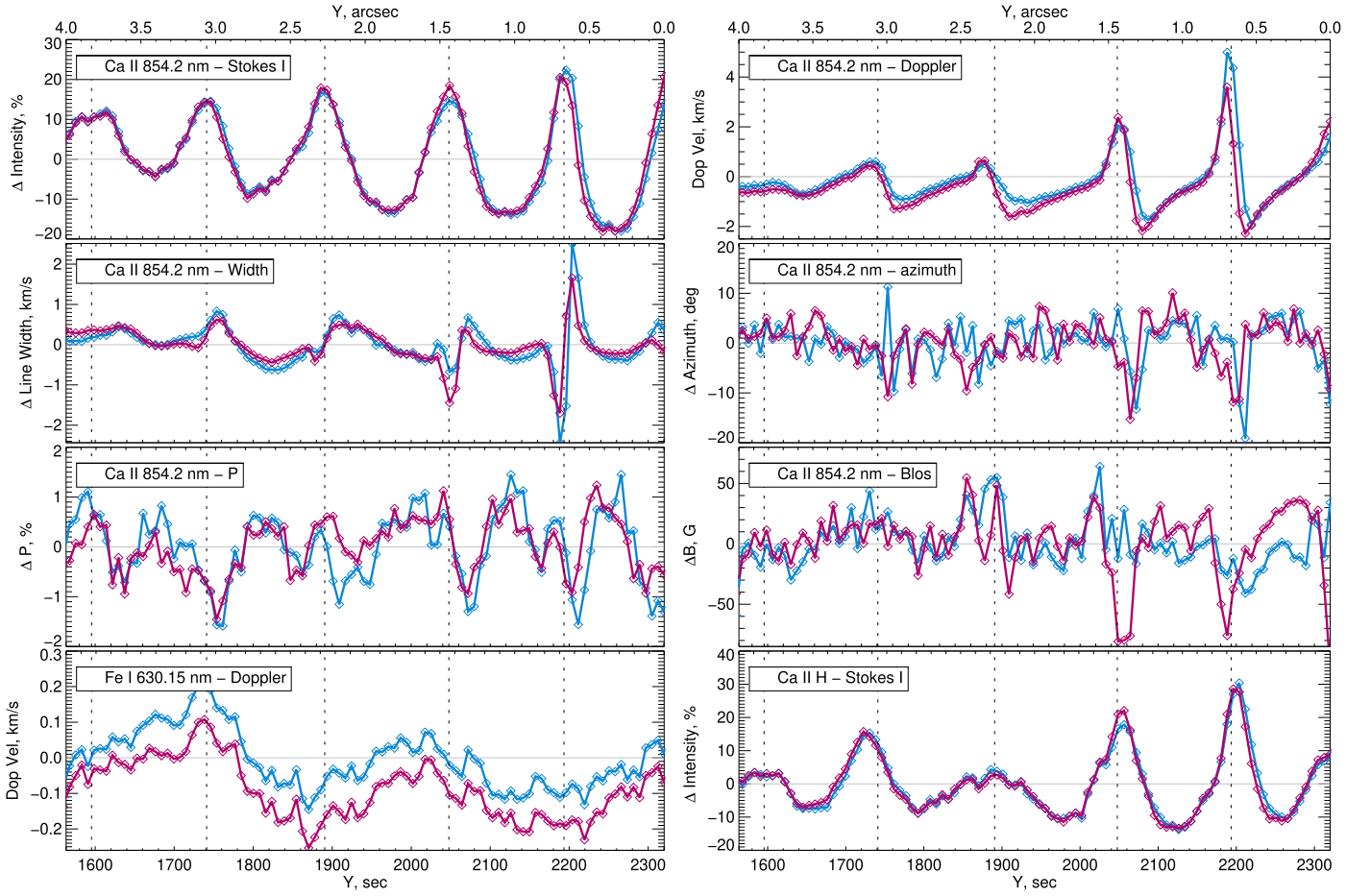
Figure 4. Detrended intensity, line width, azimuth, P, and B LOS cross sections, and raw Doppler cross sections, along the dashed cyan and magenta lines in Figure 3. The vertical dashed lines show the approximate locations of the Ca II 854 nm intensity peaks.

preshock downflow velocity of $u_+ = 11.8 \, \mathrm{km \, s^{-1}}$ and a postshock upflow velocity of $u_- = 3.83 \, \mathrm{km \, s^{-1}}$.

Suppose the shock is moving upward along the vertical magnetic flux tube, with a speed of $v \, \mathrm{km \, s^{-1}}$. In the rest frame of the shock, the ratio of the upstream to downstream velocities (and the downstream to upstream densities) is given by the usual gas dynamic Rankine–Hugoniot relations:

$$\frac{v + u_+}{v - u_-} = \frac{(\gamma + 1)M^2}{2 + (\gamma - 1)M^2} = \frac{\rho_-}{\rho_+}, \quad (5)$$

where $M = (v + u_+)/c_s$ is the upstream Mach number, c_s is the adiabatic sound speed, and γ is the ratio of the specific heats. Setting $v + u_+ = c_s M$, and defining α as $\alpha = c_s/(u_+ + u_-)$, we obtain the following expression for the Mach number:

$$M = \frac{(\gamma + 1)}{4\alpha} + \sqrt{1 + \frac{(\gamma + 1)^2}{16\alpha^2}}. \quad (6)$$

Once M is obtained, the shock velocity v is readily computed, as well as the ratio of the downstream to upstream gas pressure,

$$\frac{p_-}{p_+} = \frac{2\gamma M^2 - (\gamma - 1)}{\gamma + 1}, \quad (7)$$

and the analogous temperature ratio.

The ViSP observations give $u_+ + u_- = 15.6 \, \mathrm{km \, s^{-1}}$ for the strongest blue shock shown in Figure 4. Taking, for example, $\gamma = 1.1$, to account for Hydrogen ionization, and

$c = 10 \, \mathrm{km \, s^{-1}}$, one obtains: $M = 2.11$, $v = 9.3 \, \mathrm{km \, s^{-1}}$, $\rho_-/\rho_+ = 3.82$, $p_-/p_+ = 4.62$, and $T_-/T_+ = 1.21$. Larger sound speeds produce weaker shocks, which propagate faster; larger ratios of specific heats produce stronger shocks, which also propagate faster. The top panel of Figure 5 displays the Mach number (ordinate) for this strongest observed blue shock ($u_+ + u_- = 15.6 \, \mathrm{km \, s^{-1}}$) for a range of upstream sound speeds (c; abscissa) and several adiabatic indices (colored curves). We note that these parameters are estimates, given that the Rankine–Hugoniot relation assumes an idealized infinite planar shock propagating along a constant uniform magnetic field. The fact we see a moderate decrease in the magnetic field strength behind the shock does not invalidate these estimates.

The Stokes V and linear polarization P signals are broadly consistent with a modest expansion of the cross-sectional area of the magnetic flux tube (a decrease in the magnetic field strength), expected from the gas pressure increase behind the shock. The nominal magnetic field strength is of order 500–600 G, so $\Delta B/B \approx 0.1$. As would be expected from such an interpretation, the magnetic fluctuations are detected only for the strongest shocks.

The variation in the line width zigzag across the shock is interesting and robust. It too is most pronounced for the strong shocks, and is largely absent in the nonlinear pulses. We are presently unable to identify a compelling physical explanation for it. The dramatic change in the slope of the Doppler velocity when passing from blueshift (negative
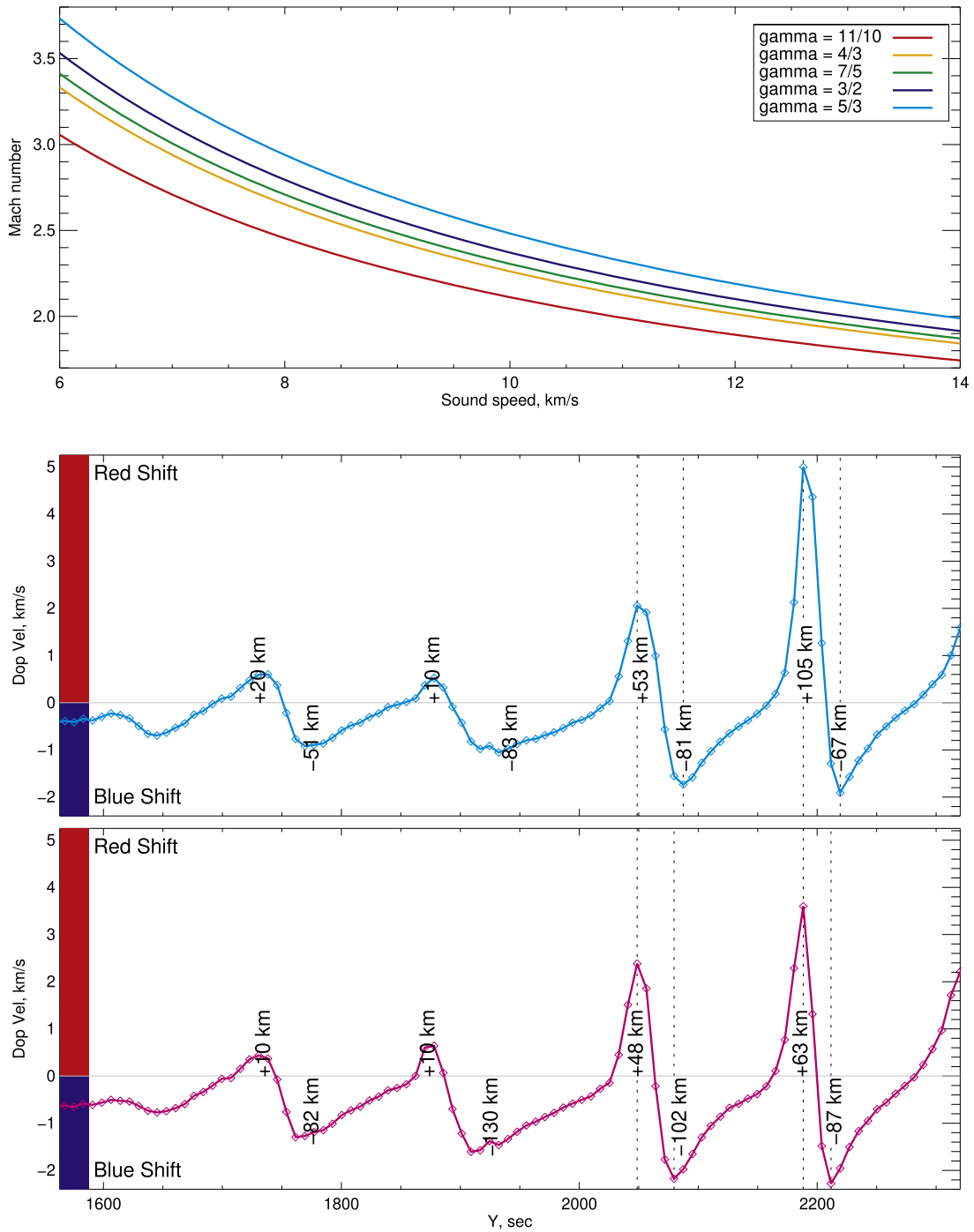
Figure 5. Top: Mach numbers of the largest shock in our observations (at $Y \approx 2200$ s in the cyan cross section), for a reasonable range of sound speed and γ values. Middle and bottom: cross sections of the Ca II 854.2 nm Doppler velocity along the cyan (middle) and magenta (bottom) cross sections in Figure 3. The dashed lines indicate the shock locations. Following time, one sees a near-constant deceleration from blueshift to redshift behind the nonlinear pulses. As the shock forms, we see increased deceleration into redshift, followed by a rapid acceleration into blueshift, before the pattern repeats into the following shock.

values) to redshift (positive values) suggests that a quasi-freefall rarefaction front may lie in between the shocks. The attendant rapid expansion of the material could lead to cooling and might also tend to stretch out, or elongate turbulent motions that are set up in the postshock flow. Both of these effects could contribute to a reduced line width. Likewise, the enhancement of the line width downstream of the shock could arise from a combination of compressive heating and postshock turbulence. On the other hand, one must acknowledge that the line source function may encompass nonequilibrium and dynamical complications, including, for example, analogous K_{2V} and K_{2R} emission processes observed in the K line. A definitive explanation of this line width zigzag will require a careful spectral synthesis.

The lack of asymmetry in Stokes I indicates that the radiative transfer in the line core is optically thick around the shock compression. The ratio of the maximum to minimum values of Stokes I is close to 3/2—the fourth root of this number is 1.10, which is comparable to, but comfortably below, our estimate for T_-/T_+ of 1.21, given above.

One can compute the integral under the undetrended Doppler velocity to determine whether there is a net flow of material along the magnetic flux tube over one cycle of oscillation. The areas (expressed kilometers) between the zero crossings of the blue and magenta curve POS Doppler velocities are provided in the bottom panels of Figure 5. We have not divided by the cosine of the inclination angle to the LOS (0.443). Taking into account this factor of 2.25, one observes that the range of upward and downward displacements per oscillation cycle is no more than a density scale height. For the weaker nonlinear pulses, there is a net upward motion of the material per cycle. However, for the strongest shock, the net motion is downward. The former behavior is consistent with the general notion that nonlinear waves contribute an upward-directed pressure gradient and tend to elevate material in a flux tube relative to its neutral hydrostatic altitude. In the latter case, where strong localized shocks are present, the precipitous quasi-freefall redshift of the material in front of the shock may carry the material farther than the subsequent upflow behind the shock. Indeed, it is tempting to speculate that, over time, the nonlinear pulses eventually raise too much plasma above its neutral level, so the subsequent formation of strong shocks in the quasi-freefall downflow is how the mature umbral flash addresses this untenable situation.

The complex projection and atmospheric refractive POS offsets between the chromospheric and photospheric oscillations make it difficult to investigate any potential photospheric roots of the umbral flash. Nevertheless, the Fe I Doppler velocity appears to attain its maximal blueshifts and redshifts close to the time of passage of the chromospheric shocks. Equivalently, the underlying photospheric oscillation has a period close to 5 minutes, or nearly twice that of the 150 s separation of the shocks in the chromosphere. This is reminiscent of the period–frequency doubling often seen in highly nonlinear systems.

4. Conclusion

In this paper, we have examined DKIST/ViSP SV observations to assess spectropolarimetric observations at high spatial and temporal resolution of chromospheric and photospheric oscillations in a sunspot, with unprecedented signal to noise. We have detected the ubiquitous running penumbral waves, chromospheric 3 minute oscillations, and an umbral flash, with the detected periods affected by the motion of the moving ViSP slit. All of these phenomena have been observed and studied for decades. However, included in the oscillation data are the Stokes V and linear polarization ($P = \sqrt{U^2 + Q^2}/I$) of the chromospheric Ca II 854.2 nm line, which provide rich spectropolarimetric signatures of the umbral flash.

Owing to residual spectrograph astigmatism at the time of the SV campaign, the data did not achieve sufficient spectral resolution to justify a detailed Stokes inversion of Ca II 854 nm. Despite these drawbacks, the SV observations provide tantalizing hints of previously unknown spatial, temporal, and spectral behaviors that are associated with the dynamical processes that are associated with a sunspot umbra. In particular, we find polarimetric evidence of a wave train of shocks and rarefactions over timescales of 0.16 s, the likes of which, to the best knowledge of the authors, have not been detected before. Across the shock train, we find values of $M = 1.88$, $v = 10.6 \, \mathrm{km \, s^{-1}}$, $\rho_-/\rho_+ = 3.15$, $p_-/p_+ = 3.66$, and

$T_-/T_+ = 1.16$. These parameters are consistent with the ranges of shock parameters calculated in other works—e.g., Anan et al. (2019).

As ViSP began science commissioning and normal operations in 2022, new observations will further push the spatial and spectral limitations of the data reported here, providing further clarity for the dynamic oscillations found within the chromosphere and photosphere.

ORCID iDs

Ryan J. French https://orcid.org/0000-0001-9726-0738
Roberto Casini https://orcid.org/0000-0001-6990-513X
Alfred G. de Wijn https://orcid.org/0000-0002-5084-4661
Philip G. Judge https://orcid.org/0000-0001-5174-0568

References

Anan, T., Schad, T. A., Jaeggli, S. A., & Tarr, L. A. 2019, ApJ, 882, 161
Balasubramaniam, K. S., Pevtsov, A. A., & Olmschenk, S. 2008, in ASP Conf. Ser. 383, Subsurface and Atmospheric Influences on Solar Activity, ed. R. Howe et al. (San Francisco, CA: ASP), 279
Bard, S., & Carlsson, M. 2010, ApJ, 722, 888
Beckers, J. M., & Tallant, P. E. 1969, SoPh, 7, 351
Besliu-Ionescu, D., Donea, A., & Cally, P. 2017, SunGe, 12, 59
Bose, S., Henriques, V. M. J., Rouppe van der Voort, L., & Pereira, T. M. D. 2019, A&A, 627, A46
Centeno, R. 2018, ApJ, 866, 89
Centeno, R., Collados, M., & Trujillo Bueno, J. 2006, ApJ, 640, 1153
Centeno, R., Collados, M., & Trujillo Bueno, J. 2009, ApJ, 692, 1211
Centeno, R., Socas-Navarro, H., Collados, M., & Trujillo Bueno, J. 2005, ApJ, 635, 670
de la Cruz Rodríguez, J., Rouppe van der Voort, L., Socas-Navarro, H., & van Noort, M. 2013, A&A, 556, A115

De Wijn, A. G., Casini, R., Carlile, A., et al. 2022, SoPh, 297, 22

Felipe, T., Socas-Navarro, H., & Khomenko, E. 2014, ApJ, 795, 9

Felipe, T., Socas-Navarro, H., & Przybylski, D. 2018, A&A, 614, A73

Felipe, T., Socas Navarro, H., Sangeetha, C. R., & Milic, I. 2021, ApJ, 918, 47

Henriques, V. M. J., Nelson, C. J., Rouppe van der Voort, L. H. M., & Mathioudakis, M. 2020, A&A, 642, A215

Houston, S. J., Jess, D. B., Asensio Ramos, A., et al. 2018, ApJ, 860, 28

Houston, S. J., Jess, D. B., Keppens, R., et al. 2020, ApJ, 892, 49

Joshi, J., & de la Cruz Rodríguez, J. 2018, A&A, 619, A63

Khomenko, E., & Collados, M. 2015, LRSP, 12, 6

Kosovichev, A. G., & Sekii, T. 2007, ApJL, 670, L147

Kuźma, B., Murawski, K., Kayshap, P., et al. 2017a, ApJ, 849, 78

Kuźma, B., Murawski, K., Zaqarashvili, T. V., Konkol, P., & Mignone, A. 2017b, A&A, 597, A133

Landi Degl'Innocenti, E., & Landolfi, M. 2004, Polarization in Spectral Lines, Astrophysics and Space Library (Dordrecht: Kluwer)

Lemen, J. R., Title, A. M., Akin, D. J., et al. 2012, SoPh, 275, 17

Lites, B. W. 1992, in Sunspots. Theory and Observations. Proc. of the NATO Advanced Research Workshop on the Theory of Sunspots, ed. J. H. Thomas & N. O. Weiss (Dordrecht: Springer), 261

Lites, B. W., Thomas, J. H., Bogdan, T. J., & Cally, P. S. 1998, ApJ, 497, 464

Löhner-Böttcher, J. 2016, PhD thesis, Albert Ludwigs University of Freiburg, Germany

Madsen, C. A., Tian, H., & DeLuca, E. E. 2015, ApJ, 800, 129

Millar, D. C. L., Fletcher, L., & Milligan, R. O. 2021, MNRAS, 503, 2444

Molnar, M. E., Reardon, K. P., Cranmer, S. R., et al. 2021, ApJ, 920, 125

Pietarila, A., Socas-Navarro, H., & Bogdan, T. 2007, ApJ, 663, 1386

Pietarila, A., Socas-Navarro, H., Bogdan, T., Carlsson, M., & Stein, R. F. 2006, ApJ, 640, 1142

Rimmele, T. R., Warner, M., Keil, S. L., et al. 2020, SoPh, 295, 172

Rouppe van der Voort, L., & de la Cruz Rodríguez, J. 2013, ApJ, 776, 56

Sadykov, V. M., Kitiashvili, I. N., Kosovichev, A. G., & Wray, A. A. 2021, ApJ, 909, 35

Schou, J., Scherrer, P. H., Bush, R. I., et al. 2012, SoPh, 275, 229

Schultz, R. B., & White, O. R. 1974, SoPh, 35, 309

Snow, B., & Hillier, A. 2021, MNRAS, 506, 1334

Socas-Navarro, H., McIntosh, S. W., Centeno, R., de Wijn, A. G., & Lites, B. W. 2009, ApJ, 696, 1683

Socas-Navarro, H., Trujillo Bueno, J., & Ruiz Cobo, B. 2000, Sci, 288, 1396

Song, D., Chae, J., Yurchyshyn, V., et al. 2017, ApJ, 835, 240

Stangalini, M., Jafarzadeh, S., Ermolli, I., et al. 2018, ApJ, 869, 110

Stangalini, M., Baker, D., Valori, G., et al. 2021a, RSPTA, 379, 20200216

Stangalini, M., Jess, D. B., Verth, G., et al. 2021b, A&A, 649, A169

Teriaca, L., Curdt, W., & Solanki, S. K. 2008, A&A, 491, L5

Thomas, J. H., Cram, L. E., & Nye, A. H. 1984, ApJ, 285, 368

Thomas, J. H., & Weiss, N. O. 2012, Sunspots and Starspots (Cambridge: Cambridge Univ. Press), doi:10.1017/CBO9780511536342

Weiss, N. O., & Proctor, M. R. E. 2014, Magnetoconvection (Cambridge: Cambridge Univ. Press), doi:10.1017/CBO9780511667459

Yurchyshyn, V., Abramenko, V., Kosovichev, A., & Goode, P. 2014, ApJ, 787, 58

Yurchyshyn, V., Kilcik, A., Şahin, S., Abramenko, V., & Lim, E.-K. 2020, ApJ, 896, 150